Boundary-Layer Meteorology
https://doi.org/10.1007/s10546-022-00707-8

RESEARCH ARTICLE

Large-Scale Turbulence Structures in the Atmospheric Boundary Layer Observed above the Suburbs of Kyoto City, Japan

Mitsuaki Horiguchi[1] · **Kenichi Tatsumi**[2] · **Alexandros-Panagiotis Poulidis**[1,4] · **Toshiya Yoshida**[3] · **Tetsuya Takemi**[1]

Received: 26 January 2021 / Accepted: 1 April 2022

Abstract

The characteristics and occurrence conditions of large-scale turbulence structures in the atmospheric boundary layer (ABL) are investigated above the suburbs of Kyoto City, Japan. An extensive observational set-up, including sonic anemometers–thermometers mounted on a tower, Doppler lidar, and radiosondes, was used to examine the turbulence structures and vertical profiles of the ABL downwind from the city. In near-neutral situations, large-scale turbulence structures with temporal scales of 100–300 s are detected by the wavelet analysis in the time series of the streamwise velocity component measured in the surface layer. A shift towards unstable conditions is found to be favourable for the emergence of large-scale turbulence structures. Furthermore, the existence of these structures is seen to be related to the development of the ABL and the change of the turbulence situation in the daytime. On average at this site, wind speed in the lower ABL increases in the afternoon. From the intensive observations, we can infer that the downward transfer of momentum via turbulent mixing and other mechanisms extends a high-speed layer at the upper levels towards the surface. Intermittent occurrence of the further increase of wind speed in an interval of several tens of minutes is also found. Turbulence structures are clearly identified in these periods of higher wind speed.

Keywords City suburb · Doppler lidar · Momentum transfer · Turbulence structures · Turbulent mixing

✉ Mitsuaki Horiguchi
horiguchi@storm.dpri.kyoto-u.ac.jp

1 Disaster Prevention Research Institute, Kyoto University, Kyoto 611-0011, Japan

2 Institute of Agriculture, Tokyo University of Agriculture and Technology, Tokyo 183-8504, Japan

3 Nuclear Science Research Institute, Japan Atomic Energy Agency, Ibaraki 319-1195, Japan

4 Institute of Environmental Physics (IUP), University of Bremen, Bremen, Germany

Published online: 25 May 2022

1 Introduction

Laboratory experiments have demonstrated the existence of well-organized and long-lived eddy structures, called coherent structures, in turbulent flows (Foken 2008). Such turbulence structures have a variety of shapes and sizes. Interest in large-scale structures has increased, since these structures are assumed to have a significant influence on the overall flow and turbulence fields. Kim and Adrian (1999) observed "very large-scale motions" (VLSMs), in the form of long regions of streamwise velocity fluctuations, in a turbulent pipe flow. The length of the VLSMs in the streamwise direction corresponds to approximately 12–14 times the pipe radius. From the wind-tunnel experiments, Hutchins and Marusic (2007) found that very long streamwise velocity fluctuations with spanwise meandering extend to over 20 times the boundary-layer thickness, and they refer to these as "superstructures".

Most laboratory experiments on coherent structures have been performed under conditions of neutral stability (no buoyancy effects) and a low Reynolds number Re (e.g. $Re \approx 10^3$ in Kim et al. 1971). In the case of the atmospheric boundary layer (ABL), the Reynolds number of the flow is very high ($Re \approx 10^8$). Therefore, the conditions of the ABL are very different from those of the laboratory experiments. The mean statistics and large-scale coherent structures in the near-neutral atmospheric surface layer (ASL) developing over the uniquely flat and smooth terrain of salt flats have been compared with those in the laboratory turbulent boundary layers (Hutchins et al. 2012). Their analysis of two-point correlation maps from the ASL indicates the presence of large-scale structures that are entirely consistent with the VLSM observed in laboratory flows.

Two mechanisms have been proposed for the generation of large-scale turbulence structures. In Hutchins et al. (2012), large-scale structures were considered to be packets or clusters of many vortices created in the layer near the surface; this is a "bottom-up" mechanism for making those structures. In contrast, from the theoretical results and experimental data, Hunt and Morrison (2000) proposed a "top-down" picture for the behaviour of turbulent eddies in the boundary layers with high Reynolds number, suggesting that large-scale eddies originally situated in the upper layer impinge onto the surface. For the typical case observed by sonic anemometers on a tower in a near-neutral ABL, Horiguchi et al. (2012) revealed a descending high-speed structure with a spatial scale of approximately 1 km at a height of 200 m, which likely corresponds to the large-scale eddies suggested by Hunt and Morrison (2000). An ascending low-speed area was also revealed to precede the high-speed structure, and the overall wind pattern was similar to the ejection–sweep structure observed by Gao et al. (1989) under unstable and near-neutral conditions for a forest canopy (mean height $\approx$ 18 m). Gao et al. (1989) operated sonic anemometers on two towers and indicated the flow structure consisting of an ejection (the slow region of upward motion) from the canopy top followed by a sweep (the fast region of downward motion) into the canopy. This ejection–sweep structure effectively contributes to the downward transfer of momentum. Vertical wind shear was considered to be a major factor in the creation of this structure.

Research interest is often directed towards the turbulence structures in a realistic setting over very rough surfaces, such as densely built cities in our living environment. Roughness elements are expected to intensify the turbulence (Grimmond and Oke 1999) and induce large-scale turbulence structures (in the bottom-up mechanism). For the ABL, the extent of the effect of rough surfaces is still under investigation. Based on a few high-quality studies of turbulence over cities, Roth (2000) argued that the roughness sublayer (the layer influenced by length scales associated with the roughness) extends to about 2.5–3 times the height of buildings for neutral conditions. In the downstream region of a large obstructing body (in the wake region), perturbations to mean flow and turbulence may reach higher levels. Park et al. (2015) investigated turbulent flow in a densely built-up area of Seoul, South Korea, using a large-eddy simulation (LES) model. Such models can handle the high *Re* flows by parametrizing the subgrid-scale turbulence. The vertical velocity variance in the selected area has a maximum value at z (vertical direction) $\approx$ 130 m, slightly above the average height of upstream buildings, and keeps still large values above $z \approx 230$ m. It is also supposed that higher roughness elements cause larger structures (Feigenwinter and Vogt 2005).

Even in the case of the flow over rough surfaces, the top-down mechanism considers the predominance of the dynamics in the outer layer (the upper part of the boundary layer) to produce turbulence throughout the boundary layer. Inagaki et al. (2017) carried out LES of a developing neutral boundary layer over a realistic building geometry of the Tokyo Area, Japan, and showed the existence of very large streaky structures extending over the boundary layer, which follow outer-layer scaling with a relevant length scale of the boundary-layer thickness. In a suburban area (Newsom et al. 2008) and an urban area (Yagi et al. 2017), streaky structures are frequently observed by the Doppler lidar. This remote sensor can detect the horizontal flow pattern in the ABL.

In the actual situation, the ABL sometimes has a structure that evolves in time. The mixed layer, in which turbulence is convectively driven in unstable conditions, reaches its maximum depth in the late afternoon (Stull 1988). Even under neutral conditions, the top-down influence of the varying conditions in the diurnal to synoptic scale on the occurrence of large-scale turbulence structures is a subject for study. As the airflow passes over the upstream area of different surface characteristics, surface inhomogeneities and topographic features become important factors for the varying conditions.

In addition to the simulations, comprehensive observations are needed to examine the real situation. However, classifying the mechanisms may be difficult using ABL observation data. Moreover, bottom-up and top-down mechanisms can simultaneously operate to create large-scale turbulence structures. The preference for one mechanism or another may also depend on the height of concern. To date, observational studies using in situ sensors have been usually confined to the lower levels in the ABL. Wang and Zheng (2016) analysed field observation data in the ASL and confirmed the existence of VLSMs. Even in this case, they supported the view that the evolution of VLSMs cannot be fully attributed to a bottom-up mechanism alone and other mechanisms, including a top-down mechanism, also probably play a role. For the study of the generation process of large-scale structures, observations up to the higher levels in the ABL are also expected.

The primary concern of this study is the occurrence conditions of large-scale turbulence structures and the mechanism of their generation in the near-neutral ABL downwind from the rough surfaces of a city. The “neutral” condition is defined as the condition under which the shear production of turbulence is much larger than the buoyant production (e.g. Stull 1988). Observations were conducted in cold and windy periods to focus on the situation of near-neutral stability. As most laboratory experiments and simulations have been conducted in neutral conditions, observational results can be compared with other results.

2 Observations and Data

2.1 Period and Location of Observations

Observations were carried out in the winter and early spring season of 2012–2013, and in the winter of 2016 at the Ujigawa Open Laboratory of the Disaster Prevention Research Institute, Kyoto University, Kyoto, Japan (34.9° N, 135.7° E). Kyoto is a large city in the main island of Honshu and lies south of the sea ($\approx$ 50 km). The laboratory is located at the southernmost portion of the urban and suburban areas that extend over approximately 14 km in the north–south direction (Fig. 1).

Kyoto has only a few tall buildings. The observation site in the suburbs of the city is surrounded by low-rise buildings and structures. For the northern area of 4 km (north–south direction) $\times$ 2 km (east–west), including the site (Fig. 1), the average fraction of the plan surface area covered by the roughness elements (λ_p) is 0.20 and the average height of the elements (z_H) is 9.8 m. These values were calculated from the digital surface model elevation data in a three-dimensional geospatial dataset (Kokusai Kogyo Co., Ltd., Tokyo, Japan). The

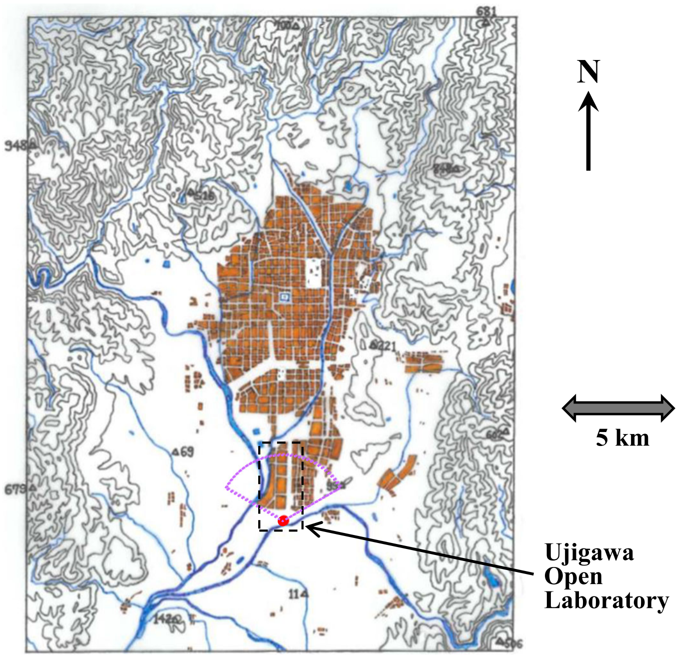

Fig. 1 Map of Kyoto City (this refers to maps drawn by the Geographical Information Authority of Japan). The contour lines represent 100-m elevation intervals. The location of the observation site (Ujigawa Open Laboratory) is shown by a red circle. The areas with buildings and structures in the city and nearby towns are depicted in brown. Parameters for roughness elements were calculated for the area enclosed by the dashed rectangle. The north direction (N) and a distance of 5 km are shown on the right of the map. The dotted sector from the site indicates the typical range of the mean wind direction for the analysed cases

packing density of roughness elements (λ_p) is comparatively low in the normal range (0.1–0.6) for cities (Grimmond and Oke 1999). In order to classify the landscape of the site, a local climate zone (LCZ) system (Stewart and Oke 2012) can be used. A class of LCZ 8 (large low-rise built type) is suitable for the rectangular area in Fig. 1. The aerodynamic roughness length (z_0), which is another measure of the roughness, will be obtained from the observations (Sect. 3.1).

In this place, a northerly wind is optimum for the measurement of the flow over the city. For the area in Fig. 1, the ratio of the total frontal area of the roughness elements, which face north, to the plan surface area is 0.12. This value of the frontal area index (λ_f) is also low considering the lower limit (0.05) of real cities (Grimmond and Oke 1999).

2.2 Equipment

The site has a meteorological tower 55-m tall. Observations of turbulence in the surface layer were carried out using sonic anemometer–thermometers (DA-600, Kaijo Co., Tokyo, Japan) (hereafter simply referred to as sonic anemometers). Horizontal axes for wind measurements were configured in the front part of the probe (TR-61A) to reduce the influence of the structural supports or transducers. Two sonic anemometers were set up on the tower at 25-m and 40-m levels with their probes facing northward. Only cases with a deviation of the mean wind direction less than 60° from true north were typically used. In this span of the direction, roughly flat surfaces continue for more than 3 km northwards from the site (Fig. 1). This probe orientation is also suitable for the observations of winter seasonal winds, which blow from the north. One vertical and two horizontal velocity components with the sonic virtual temperature were sampled every 0.1 s. The sonic virtual temperature slightly depends on water vapour pressure. In the following analysis, the effect of water vapour was neglected because the air temperature and humidity during the observations were low.

In January and February 2016, a Doppler lidar unit (WINDCUBE WLS-7, Leosphere, Orsay, France) was also used for observation of the wind in the lower ABL (cf. Cañadillas et al. 2011). This instrument measures the Doppler shift of laser radiation backscattered by particles in the air approximately every second for each beam direction and obtains three-dimensional wind components from conical scanning with four azimuth angles over a height range of 40–220 m (20-m intervals). From the observations, real-time acquisition and 10-min average data are stored. Specifications of the Doppler lidar are summarized in Table 1.

A verification test of the same type of Doppler lidar was performed by Gottschall and Courtney (2010). They reported satisfactory results for the average data. In Gottschall and

Table 1 Specifications of the Doppler lidar

Item	Specification
Height range	40–220 m
Range resolution	20 m
Beam geometry	4 inclined beams at 15°
Data sampling rate	1 Hz
Output data (main items)	Real-time acquisition (three velocity components) 10-min average (wind speed, wind direction, vertical component of the wind vector)

Courtney (2010), the lidar error was defined as the wind speed measured by the Doppler lidar minus the reference wind speed measured by the cup anemometer on the meteorological mast. The standard deviations of the lidar error at five heights (40 m, 60 m, 80 m, 100 m, 116 m) were smaller than 0.1 m s^{-1}. However, it should be noted that wind fluctuations are not adequately represented in the original real-time observation data (Cañadillas et al. 2011; Yoshida et al. 2018). For example, Cañadillas et al. (2011) pointed out that the power spectrum for the wind speed from the Doppler lidar measurements presents a signal increase compared to the power spectrum from the sonic anemometer measurements at frequencies between 0.004 and 0.2 Hz.

Additionally, for the measurements over the ABL, radiosondes (RS-11G, Meisei Electric Co., Ltd., Gunma, Japan) were launched five times during the daytime on 2 and 3 February 2016. The radiosondes transmitted data for air temperature, relative humidity, and global position every second (corresponding to height intervals of several metres). Wind speed, wind direction, and air pressure were immediately calculated from the received signals.

2.3 Data Preparation

For the analysis of turbulence structures, near-neutral cases were selected. The surface-layer scaling parameter, which is the ratio of the observation height z to the scaling (Obukhov) length L, was used for the stability criterion

$$z/L = -\frac{\left(g/\overline{T}\right)\left(\overline{w\prime T\prime}\right)}{u_*^3/kz},$$

where g is the acceleration due to gravity, T is the air temperature, w is the vertical velocity component of wind (positive upwards), u_* is the friction velocity, and k (= 0.4) is the von Kármán constant (cf. Stull 1988). The overbar denotes the mean component, and the prime denotes the fluctuation component (from the mean). The covariance $\overline{w'T'}$ represents the eddy flux of heat. The friction velocity is a velocity scale and defined to represent the effect of wind stress τ,

$$\tau = \rho u_*^2$$

where ρ is the air density. The magnitude of τ can be estimated according to $\tau = -\rho\overline{u'w'}$ (the Reynolds shear stress), where u is the velocity component in the mean wind direction (the streamwise velocity component). In the above, it is assumed that stress and velocity vectors are aligned in the same direction, and $\rho\overline{u'w'}$ is the eddy flux of streamwise momentum. The scaling parameter z/L is nearly equivalent to the flux Richardson number (R_f), which is the ratio of the buoyant production term to the shear production term in the budget equation of turbulence kinetic energy. The sign of z/L relates to static stability: negative implies unstable, and positive implies stable (Stull 1988).

At this site, eddy fluxes were measured by a sonic anemometer and mean temperature ($\overline{T}$) was evaluated by a quartz thermometer (sensor TS-709, Ogasawara Keiki Co., Ltd., Tokyo, Japan) on the tower. The stability was usually evaluated using the data obtained at the 40-m level. For observations in 2016, the data at 25 m were used owing to the incorrect response of the 40-m sonic anemometer during this period.

The mean wind vector may not be situated in the horizontal plane by the effects of surface roughness elements. Therefore, for the analysis of flux, which is sensitive to the choice of the reference frame, the u velocity component was taken in the three-dimensional mean wind direction. The w component was then taken in the upward direction normal to the mean wind direction. In a right-handed coordinate system, the lateral velocity component (v) is taken in the direction normal to the directions of the u and w components.

For the survey of the whole dataset, recorded data were divided into 30-min data segments (hereafter referred to as parts). An analysis of time-averaged statistics was applied to each part. The mean wind direction, mean u ($\overline{u}$), values of covariance, u_*, $\overline{T}$, and z/L were calculated. Each observational case was defined as a series of measurements during 210 min (seven parts), in which the surface layer was near-neutral. Such a long period is adopted for the detection of many turbulence structures. Stability parameters in the range of $-0.2 < z/L < 0.2$ were considered to be near neutral. When near-neutral situations continued longer than 210 min, the period with the smallest summation of $|z/L|$ was selected. As described in Sect. 3.2, turbulence data during 1 day, in which the stability was sometimes near neutral, were used for the examination of diurnal variation.

Stability of the flow in the ABL beyond the surface layer is evaluated using the gradient Richardson number Ri,

$$Ri = \frac{\left(g/\overline{\theta}\right)\left(\partial\overline{\theta}/\partial z\right)}{\left(\partial\overline{U}/\partial z\right)^2},$$

where θ is the potential temperature, and U is the wind speed. The components in Ri can be measured by the radiosonde. This parameter represents the relative importance of buoyancy and shear in producing turbulence (cf. Kaimal and Finnigan 1994).

2.4 Data Analysis Method of Wavelet Transform

To extract the specific structures from the turbulence data, an integral wavelet transform (cf. Kronland-Martinet et al. 1987) was applied to the time series, e.g. $x(t)$, where t is time. The wavelet transform $T(a,b)$ with a scale parameter a and a translation parameter b is calculated as follows

$$T(a,b) = \left(\frac{1}{a}\right)\int_{-\infty}^{+\infty} \Psi\left(\frac{t-b}{a}\right)^* x(t)\mathrm{d}t,$$

where $\Psi(t)$ is an analysing wavelet. The asterisk denotes the complex conjugate of the function. The scale parameter a alters the length and amplitude of the wavelet, and the translation parameter b sets the location of the wavelet.

The value of the wavelet transform depends on the shape of the analysing wavelet. As in previous studies on the turbulence in the ABL (Gao and Li 1993; Chen and Hu 2003), the Mexican hat wavelet function was employed. This function is given by

$$\Psi(t) = \left(1-t^2\right)\exp\left(-t^2/2\right),$$

which is well localized in both time and frequency with a smooth and symmetrical shape. The wavelet transform can detect intermittent variations in the time series. As will be seen in Sect. 3.1, the above function is suitable for the extraction of turbulence structures, which show the gradual change of the velocity component. The time scale defined by $2a$ was used for sorting turbulence structures according to their scale.

Additionally, for the examination of the representative scale of structures, the wavelet variance spectrum $W(a)$ (Mahrt 1991; Collineau and Brunet 1993) was calculated as follows

$$W(a) = \int_{-\infty}^{+\infty} |T(a, b)|^2 \mathrm{d}b.$$

In this study, the wavelet variance was examined up to the time scale of 352 s, which is sufficient to detect large turbulence structures. As will be seen in the next section, in contrast to the power spectrum using the Fourier transform, the wavelet variance spectrum can indicate a clear maximum. This difference probably derives from the high resolution of the wavelet spectrum in the range of low frequency (large time scale).

3 Results and Discussion

3.1 Turbulence in the Near-Neutral Surface Layer

General features of the turbulence structures in the near-neutral surface layer at this site are investigated in this subsection.

After the inspection of all the sonic anemometer data during December 2012 to March 2013, 30 near-neutral cases were obtained and are referred to here as cases 1–30 (Table 2). The synoptic weather map by the Japan Meteorological Agency (JMA) was examined for the observation days. A winter pressure pattern, in which high pressure lies to the west of Japan, or the eastward movement of a low pressure system was seen on most days. Average values of wind speed, friction velocity (u_*), and the surface-layer scaling parameter (z/L) for each case were evaluated at the 40-m level (Table 2). The ranges of the wind speed and friction velocity were 3–9 m s^{-1} and 0.2–0.8 m s^{-1}, respectively. A logarithmic wind profile, $\overline{u}(z) = (u_*/k) \ln(z/z_0)$, was assumed to calculate the roughness length z_0 from the mean u and the friction velocity. The values of z_0 in the range of 0.1–1.7 m were obtained from the 30 cases. These values are not dependent on the wind direction. The average value of z_0 was 0.7 m, with large variability among cases, which is comparable to typical values for natural woodland surfaces (cf. Garratt 1994).

To investigate the turbulence properties in the surface layer, normalized velocity standard deviations of wind were examined. These deviations are used for the estimation of turbulence intensities and defined as

$$A_i = \sigma_i / u_* (i = u, v, w),$$

where σ is the standard deviation of the velocity component (Roth 2000). For this analysis, a three-dimensional coordinate transformation was applied to the wind components. The ranges of A_u, A_v, and A_w at the 40-m level were 2.1–3.1, 1.8–3.0, and 1.3–1.9 for the 30 cases. These values are slightly larger than the representative values of 2.32 $\pm$ 0.16, 1.81 $\pm$ 0.20, and 1.25 $\pm$ 0.07, respectively, for neutral stability at $z_s/z_H > 2.5$ from the selected urban studies (Roth 2000), where z_s is the height of the sensor above ground. In this study $z_s/z_H = 4.1$. As the rural reference data are very similar to the above urban averages, with differences of less than 10% (Roth 2000), the roughness elements surrounding this site have some effect on the intensity of turbulence.

Table 2 Average values of wind speed, friction velocity (u_*), and surface-layer scaling parameter (z/L) at 40 m for the observation cases

Case	Date	Time (LST)	Horizontal wind speed (m s^{-1})	Friction velocity, u_* (m s^{-1})	z/L	Peak time scale of wavelet variance spectrum (u, 40 m) (s)	
						Global maximum	Local maximum
1	21 December 2012	1930–2300	4.5	0.33	0.05	64	
2	22 December 2012	1630–2000	5.5	0.43	0.06	–	36
3	26 December 2012	0630–1000	6.2	0.53	− 0.05	40	
4	26 December 2012	1800–2130	3.5	0.38	− 0.03	204$^+$	56
5	6 January 2013	1800–2130	3.7	0.24	0.04	84	
6	9 January 2013	1630–2000	5.0	0.42	0.07	32	128$^+$
7	17 January 2013	1730–2100	3.8	0.38	− 0.02	228$^+$	
8	18 January 2013	0430–0800	4.7	0.46	− 0.02	28	60, 292$^+$
9	20 January 2013	1600–1930	4.1	0.42	− 0.04	–	164$^+$
10	22 January 2013	1600–1930	5.2	0.44	0.02	80	
11	26 January 2013	1730–2100	4.6	0.49	− 0.02	100$^+$	
12	3 February 2013	0130–0500	4.7	0.45	0.03	–	64
13	5 February 2013	0430–0800	4.6	0.38	0.02	52	160$^+$
14	5 February 2013	1500–1830	5.2	0.47	− 0.12	224$^+$	40
15	6 February 2013	0130–0500	3.3	0.31	0.01	–	60, 164$^+$
16	8 February 2013	0300–0630	5.9	0.54	− 0.03	96	300$^+$
17	16 February 2013	0200–0530	7.0	0.51	0.01	36	92
18	19 February 2013	0230–0600	5.9	0.55	0.03	92	
19	19 February 2013	1630–2000	3.8	0.36	− 0.08	100$^+$	
20	20 February 2013	1700–2030	4.5	0.47	0.03	68	
21	27 February 2013	0100–0430	3.6	0.30	− 0.06	52	280$^+$

Table 2 (continued)

Case	Date	Time (LST)	Horizontal wind speed (m s^{-1})	Friction velocity, u_* (m s^{-1})	z/L	Peak time scale of wavelet variance spectrum (u, 40 m) (s)	
						Global maximum	Local maximum
22	1–2 March 2013	2200–0130	7.9	0.72	0.01	76	
23	3 March 2013	1600–1930	5.7	0.54	− 0.04	152$^+$	
24	10 March 2013	1730–2100	5.8	0.59	− 0.01	156$^+$	
25	13 March 2013	2000–2330	9.1	0.72	− 0.02	108$^+$	292$^+$
26	14 March 2013	0330–0700	8.3	0.78	0.00	72	
27	14 March 2013	1700–2030	5.0	0.46	− 0.05	108$^+$	340
28	16 March 2013	1900–2230	6.0	0.50	0.04	120$^+$	28, 308
29	21 March 2013	0430–0800	5.7	0.54	− 0.01	–	80
30	23 March 2013	0530–0900	4.7	0.45	− 0.10	96	

The time scale of the peak in the wavelet variance spectrum for the u component at 40 m is also shown. Dashes (–) denote cases when the wavelet variance increases at large time scales

$^+$ Peak of the wavelet variance spectrum within the large-scale range (100–300 s)

As an example of turbulence data, Fig. 2 shows the time series of u and w velocity components measured by the sonic anemometers at the 25-m and 40-m levels during 1800–1830 local standard time (LST, which is UTC + 9 h) on 26 December 2012 (part 1 in case 4). This represents typical large-scale turbulence structures: strong wind events with a time scale of 100–200 s are recognized in the small-scale fluctuations of the u component. A corresponding change to the u component is sometimes found in the w component. For example, in advance of a strong wind event at 1804 LST, a region of upward velocity was observed at both heights.

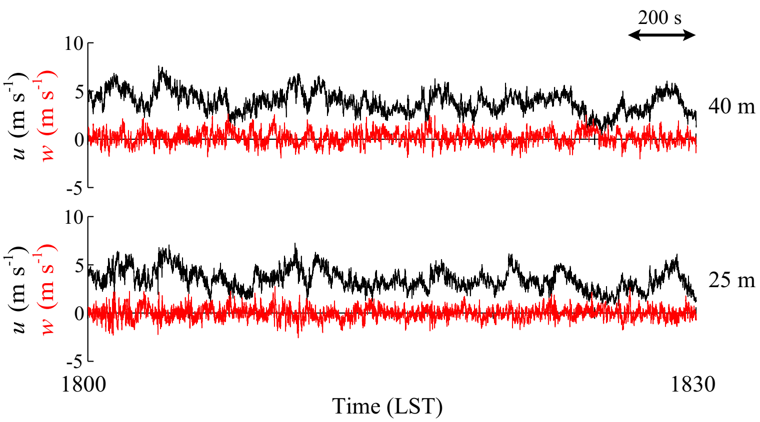

Fig. 2 Time series of u (black) and w (red) velocity components as measured by sonic anemometers for part 1 (1800–1830 LST) of the observation case during 1800–2130 on 26 December 2012. The time scale for 200 s is also shown

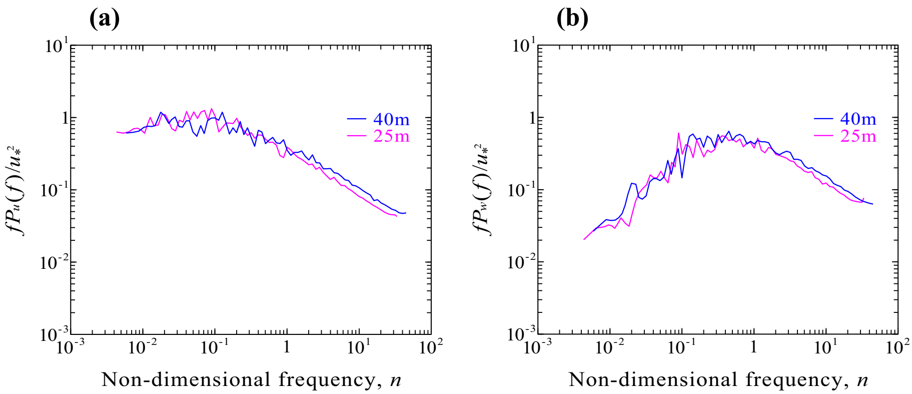

Fig. 3 Power spectra for the u (**a**) and w (**b**) velocity components in the observation case during 1800–2130 LST on 26 December 2012. Frequency (f)-weighted power spectra for the u and w components (P_u and P_w, respectively) for each part were normalized with respect to $u_*{}^2$ and represented as a function of non-dimensional frequency n ($= fz/\overline{u}$). These spectra were then averaged over parts 1 to 7. The scatter in spectral estimates was reduced by smoothing with a frequency window after Kaimal and Finnigan (1994)

Frequency (f)-weighted power spectra for the u and w velocity components of case 4 are shown in Fig. 3 as a function of non-dimensional frequency n ($= fz/\overline{u}$). A three-dimensional coordinate transformation was applied to the wind components. Spectral peaks are located at approximately 0.1 and 0.4 for the u and w components, respectively. This is similar to the previous results for the velocity spectra in a surface layer under neutral stability (e.g. Kaimal and Finnigan 1994). Roth (2000) pointed out that the peak frequency for the w spectrum in an urban area is systematically lower than the rural reference. Partly because of the large scatter in the original spectra, the effect of the roughness elements is not discernible for all cases observed at this site.

A wavelet transform was applied to the series of the streamwise velocity component (u) at each level. For this analysis, the u component was taken in the direction of the mean wind at the 40-m level and in the horizontal plane. This procedure makes it possible to detect the change of the wind in one direction. Fluctuations normalized with respect to the standard deviation in each part were used, taking into consideration the gradual change in wind conditions. Moreover, block averaging of every 20 data points was applied to diminish fine-scale variations, and the average values were then connected over the seven parts.

Figure 4 shows an example of wavelet variance spectra for the u velocity components observed at the two levels in case 4 (1800–2130 LST, 26 December 2012). These spectra

Fig. 4 Wavelet variance spectra for the u velocity component as a function of the time scale (observation case during 1800–2130 LST on 26 December 2012)

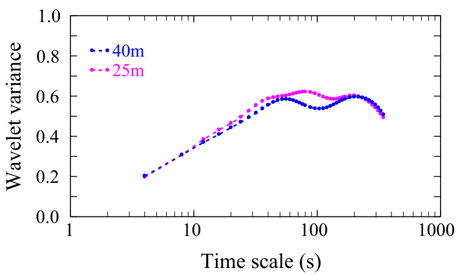

indicate that peaks are located at the time scales of 80 and 196 s for the 25-m level, and 56 and 204 s for the 40-m level. Strong wind events as in Fig. 2 contributed the spectral peaks in the large time scale of more than 100 s. For all cases, wavelet variance spectra for the *u* component at 40 m were examined (Table 2). In the table, the global maximum is the largest value in the spectrum, while the local maximum is larger than the values of only the neighbouring points. Since the local maximum coexists with the larger values in the spectrum, multiple peaks can be present. In the cases denoted by a dash (–), the wavelet variance kept increasing in the region of the large time-scale (i.e., no global maximum was found). In these cases, very large velocity variations exist in the turbulent flow.

In Table 2, the peak of the wavelet variance spectrum within the time-scale range of 100–300 s is indicated by a plus mark (+). In the present analysis, this range is defined as indicating a "large-scale" turbulence structure, as used in Horiguchi et al. (2014). A spectral peak located in this range indicates that large-scale turbulence structures predominantly exist in the time series of the *u* velocity component. As shown in Table 2, the spectral peak in the large-scale range (100–300 s) is not always found. Case 3 (0630–1000 LST, 26 December 2012) is an example, in which a global maximum of the spectrum is located at the time scale of 40 s. The spectrum for the *u* component at 40 m exhibits a global maximum in the large-scale range for 10 cases and a local maximum in this range for 8 cases. Because both global and local maxima are found in case 25, single or multiple peaks in the large-scale range can be found for 17 cases in total.

We observe the turbulence structures in a flow of the mean wind speed, which pass over a fixed point of the site. In the global maximum cases, the standard deviation of u (σ_u) is small compared with the mean u ($\overline{u}$): $\sigma_u < 0.32\,\overline{u}$ for these cases. The spatial scale of the large-scale turbulence structures can be estimated from the time scale of the peak in the wavelet variance spectrum. The time scales of the spectral peaks (100–228 s) for the global maximum cases convert into the spatial scales in the range of 380–1,150 m from the average values of $\overline{u}$ at the 40-m level in each case (3.4–9.0 m s $^{-1}$). More specifically, the maximum spatial scale of the predominant turbulence structures is of the same order of magnitude as the maximum depth of the ABL over the land surface in the daytime (cf. Arya 2001).

As mentioned above, a predominance of large-scale turbulence structures is not always observed. Upwind surface characteristics affect the turbulent flow in this place. However, we could not find the dependence of turbulence structures on the wind direction. We examined other factors. First, properties of the wavelet variance spectrum in relation to the deviations from the (strictly) neutral stability were investigated. In many cases (13 cases), a global maximum or a local maximum in the large-scale range is found under slightly unstable conditions ($z/L < 0$). This indicates that a stability shift towards unstable conditions is favourable for the emergence of large-scale turbulence structures. A similar result was obtained from an analysis of the turbulence data measured at the 200-m height on a meteorological tower in Tsukuba City, Japan (Horiguchi et al. 2014).

Another noteworthy feature of the cases in which a global maximum was found in the large-scale range is the observation time in the day. The beginning times of these cases were during the late afternoon to early evening (1500–2000 LST). Here, normal diurnal changes in the stability condition should also be taken into consideration. In the early morning and the period from late afternoon to early evening, the stability in the ABL is likely to be near neutral. As expected, the observation time for 30 near-neutral cases was confined to before 1000 LST or after 1500 LST. Even so, because all global maximum cases occurred in the afternoon, the predominance of large-scale turbulence structures is possibly related to the diurnal evolution of the ABL. In fine weather, the depth of the ABL (mixed layer) usually increases in the daytime until late afternoon (cf. Stull 1988). Although observations in this study were conducted during the cold season, some growth of the ABL in depth and variations of its structure are likely to occur. The turbulence situation in the ABL may also change during the course of a day. In connection with the evolution of the ABL, the predominance of large-scale turbulence structures is observed in many types of synoptic pressure pattern.

This study suggests that top-down influence causes large-scale turbulence structures. This means that large contributions are made by the surrounding conditions, including the stability and vertical structure of the ABL.

3.2 Diurnal Variation of the Wind Speed and Turbulence Structures in the Boundary Layer

To further study the overall impact of large-scale turbulence structures and examine their links to diurnal changes in the ABL, Doppler lidar and radiosonde observations were carried out. This subsection describes the investigation of a specific day, 3 February 2016. On this day, a winter pressure pattern of Japan was seen in the synoptic weather map by the JMA, and stronger wind speeds were observed at the site in Kyoto.

3.2.1 Diurnal Variation of the Wind Speed in the Boundary Layer

Figure 5 shows the mean wind direction, surface-layer scaling parameter (z/L), friction velocity (u_*), and mean of the streamwise velocity component (u) at the 25-m level for 30-min

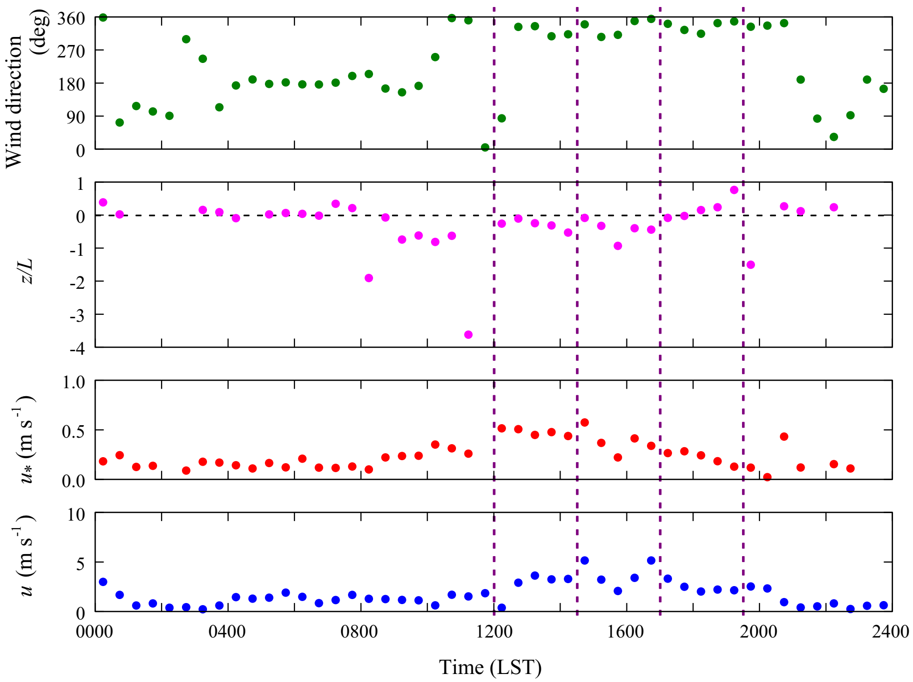

Fig. 5 Mean wind direction, surface-layer scaling parameter (z/L), friction velocity (u_*), and mean of the streamwise velocity component (u) at 25 m for 30-min data segments on 3 February 2016. Blanks for z/L and u_* are when $\overline{u'w'}$ is positive or z/L is out of range. Subcases in the afternoon are shown by dashed lines

data segments (parts) on 3 February 2016. Visual observations at this site showed the weather to be cloudy in the morning and fine in the afternoon. The maximum surface air temperature, as obtained from 10-min averages measured by the same instrument as on the tower, was 8.2 °C. On this day, the stability in the surface layer was sometimes near neutral ($|z/L|< 0.2$) (Fig. 5).

Inspection of Fig. 5 shows that southerly winds were accompanied by stable or near-neutral situations in the early morning. Unstable or near-neutral situations were present after 0800 LST (more frequently near neutral in the afternoon), and the wind direction changed to northerly after 1030 LST. From 1830 LST, stable conditions returned. The friction velocity, which is related to the magnitude of downward momentum flux, gradually increased and reached a maximum in the afternoon (1430–1500 LST). Wind speed (the u component) also increased in the afternoon and peaked ($\overline{u} = 5.1$ m s^{-1}) at 1430–1500 and 1630–1700 LST. High wind speed continued until evening. The wind speed in the surface layer usually increases after sunrise and attains a maximum in the afternoon, which is explained by momentum transfer due to convective mixing (Crawford and Hudson 1973). At this site, the increase of wind speed in the afternoon is known from monthly mean data from the windmill anemometers at 25-m, 40-m, and 55-m levels on the tower. Even in the cold season of February, this tendency is evident. The 1-h average wind speed of 2.6 m s^{-1} during 0900–1000 LST at 25 m increases up to 4.4 m s^{-1} during 1500–1600 LST, which is based on the data from the year 2005 to 2015. Jiménez et al. (2016) analysed wind observations taken at a tower and showed higher winds in the daytime near the surface for all seasons. Some type of turbulent mixing contributes to the vertical transfer of momentum in winter.

Figure 6 shows the 10-min averages of wind speed in the lower ABL observed by a Doppler lidar. The wind speed gradually increased from the late morning. At the highest level (220 m), average wind speed increased to more than 4 m s^{-1} during 1230–1240 LST and high wind speed continued afterwards. In the afternoon, further strong winds over the deep layer were sometimes observed. Abrupt intensification of wind speed at around 1430 LST occurred simultaneously at all observation levels. Based on the same average data, wind directions at almost all levels were northerly from 1020 LST until the late evening. On this day, the Doppler lidar observations showed that a maximum speed of 8.9 m s^{-1} was attained during 1440–1450 LST at the 200-m level. The occurrence interval of further intensification, which was derived from the local maxima of wind speed at 220 m, was 30 to 50 min in the period 1200–1700 LST.

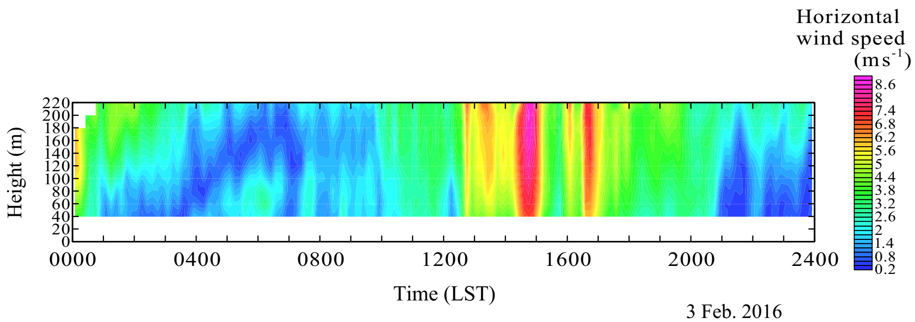

Fig. 6 Wind speed in 10-min averages, as observed by a Doppler lidar on 3 February 2016

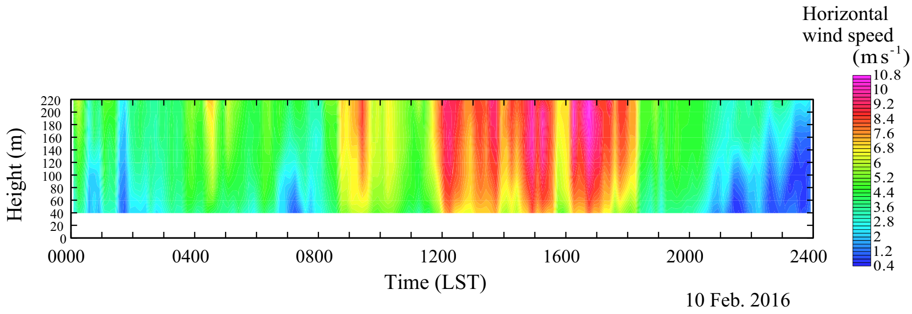

Fig. 7 Wind speed in 10-min averages, as observed by a Doppler lidar on 10 February 2016

The increase of wind speed in the afternoon and the intermittent occurrence of further intensification over the deep layer in the lower ABL were found also on other days by the Doppler lidar. For example, Fig. 7 shows the wind speed in 10-min averages observed on 10 February 2016. The weather was mostly fine in the daytime. The wind was westerly or northerly, and the stability was usually near neutral or unstable until the evening. On this day, high wind speed continued in the afternoon and attained a maximum value of 10.7 m s^{-1} during 1640–1650 LST at the 200-m level. In addition, further strong winds over the deep layer were frequently observed in the afternoon also on 10 February 2016. The occurrence interval derived in the above manner is 20 to 50 min in the period 1200–1700 LST.

The Doppler lidar also measures the vertical component of the wind vector. In addition to the wind speed, the standard deviation of the vertical components every 10 min was examined from the averaged data. This value represents the vertical fluctuations of the airflow, which induce turbulent mixing. On 3 February 2016, the standard deviation increased after approximately 1000 LST prior to the increase of wind speed. The maximum value was 1.1 m s^{-1} during 1250–1300 LST at the 200-m level. This result reflects the early evolution of the turbulence situation in the ABL, which was also seen on 10 February 2016.

Figure 8 shows the vertical profiles of wind speed, which were observed by radiosondes. The profiles are shown with the vertical axis referenced to the height above mean sea level (the altitude of the Ujigawa Open Laboratory is 11 m). At heights below 1 km, wind speed increased in the afternoon. For example, at around the 200-m height, wind speed increased from 1.4 m s^{-1} at 1200 LST to 4.1 m s^{-1} at 1400 LST. This change corresponds to the increase of wind speed in the afternoon over the layer observed by the Doppler lidar (Fig. 6). The radiosonde can observe the wind up to the higher level. Unlike the decrease of wind speeds in the daytime at upper levels (several hundred metres in height) on an averaged basis (Crawford and Hudson 1973; Mahrt 1981), wind speeds in the present case (winter seasonal winds) increased in the afternoon over the whole layer below 1 km.

As air density is derived from air pressure and temperature, horizontal momentum can be calculated from the radiosonde observations. From the surface to a height of 1 km, the average momentum of 2.8 kg m^{-2} s^{-1} (per unit volume) changed to 6.8 kg m^{-2} s^{-1} in the period 1200–1400 LST. In contrast, at greater heights, strong winds were experienced from the morning. For the layer from 1.0 to 1.9 km, the average momentum was 12.1, 8.6, and 9.2 kg m^{-2} s^{-1} at 0900, 1030, and 1200 LST, respectively. Large values of momentum continued (10.6 and 8.0 kg m^{-2} s^{-1} at 1400 and 1600 LST, respectively) in the afternoon. For all radiosonde observations, wind directions at heights above 400 m were almost northerly up to the height of 2 km.

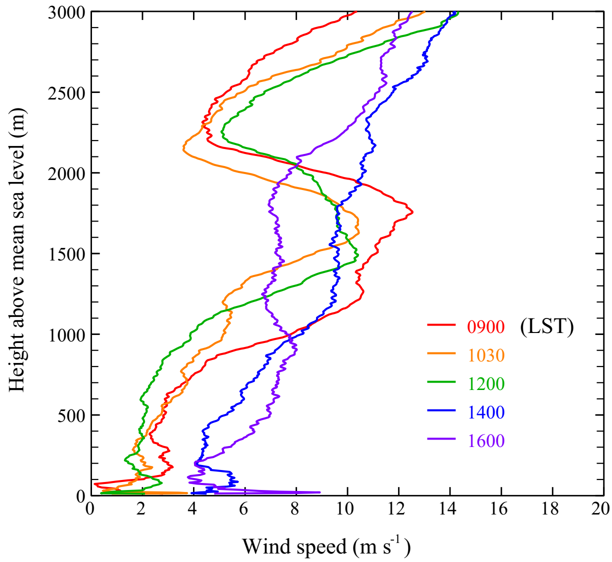

Fig. 8 Vertical profiles of wind speed observed by radiosondes on 3 February 2016. The profiles are shown with the vertical axis referenced to the height above mean sea level

The above observations suggest that the increase of wind speed in the afternoon is related to the evolution of the ABL. Radiosondes also observed the vertical profiles of air temperature. The profiles of potential temperature (θ) (from air temperature and pressure) for all observations of 0900–1600 LST show a layer of small vertical gradients, the depth of which was around 2 km (Fig. 9). This layer was presumably a residual of the convective mixed layer induced by the cold air outbreaks from the north over the Sea of Japan (cf. Lenschow et al. 1980).

In spite of the similar profiles for all observations, the approximate depth of the well-mixed layer changed from 1.9 or 2.0 km in the morning and at noon to 2.3 km in the afternoon (Fig. 9). Moreover, the vertical gradient of potential temperature also changed. To ascertain this aspect, average potential temperatures from the 1.0-km to 1.9-km height were compared with those from the surface to the 1.0 km height. The potential temperature increment of 1.7 K at 0900 and 1.4 K at 1030 LST in the upper layer decreased to 0.8 K at 1200, 0.7 K at 1400, and 1.0 K at 1600 LST. A well-mixed layer definitely developed towards afternoon. As seen above, the observational results of wind speed and temperature by radiosondes indicate the diurnal evolution of the ABL.

From all observations described thus far, we can infer that large turbulent mixing and the resultant transfer of momentum in the daytime extends the high-speed layer at the upper levels towards the surface. The increase of downward momentum flux in the afternoon was verified by the sonic anemometer measurements in the surface layer (Fig. 5). The wind speed at a height near 1 km observed by radiosondes in the afternoon corresponds well to that in the further intensification in the interval of several tens of minutes observed by the Doppler lidar. This suggests the sporadic intrusion of a fast-moving upper layer to the lower ABL.

The time scale of the intermittent increase of wind speed (30–50 min on 3 February 2016) is situated in what is called the gap range. By making a spectral analysis of wind speed, Van der Hoven (1957) showed that a spectral gap (a region of small power) is centred at

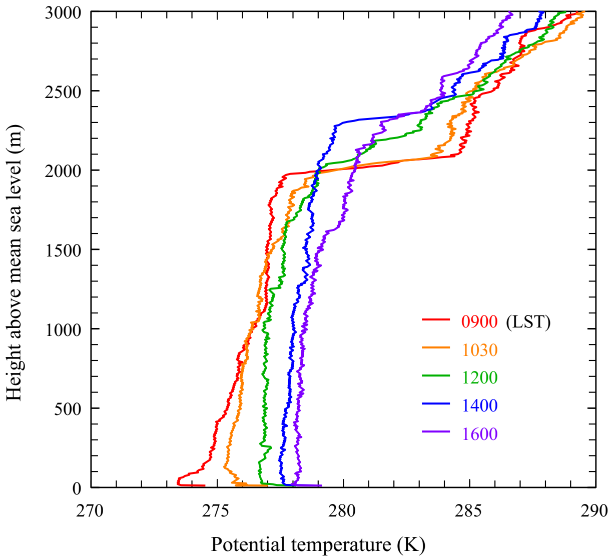

Fig. 9 Vertical profiles of potential temperature observed by radiosondes on 3 February 2016. The profiles are shown with the vertical axis referenced to the height above mean sea level

a frequency ranging from 1 to 10 cycles per hour. Larsén et al. (2016) defined four ranges to cover the full-range spectrum: macroscale, mesoscale, gap range (frequency of about 2 $\times$ 10^{-4} to 2 $\times$ 10^{-3} Hz), and microscale (higher than about 10^{-3} Hz). In reality, wind variation with a time-scale in the gap range also exists. For example, Novitskii et al. (2011) noted that the turbulence characteristics measured in the surface layer of the coastal area reveal a temporal variability with the typical scale of about 1 h regardless of the atmospheric stratification.

Under the conditions studied here, the transfer of momentum in the ABL occurred during the passage of the wind over surfaces in the city. Under near-neutral situations, this process is attributable to turbulent mixing by wind shear. Certainly, it takes a very long time to obtain high wind speeds near the surface by convergence of momentum flux. Thus, additional mechanisms for the wind speed variations are considered. Large-scale turbulent flow behind the buildings in the upwind area may induce a large momentum transfer (cf. Park et al. 2015). This impact does not change much throughout the day. Because the surface layer was sometimes unstable in the afternoon, buoyancy effects may be important for the vertical mixing.

Stability of the flow in the ABL was examined by using the gradient Richardson number (Ri), which was obtained by the radiosonde observation. Owing to the large variability of measurement data in the original profiles, average values of wind speed and potential temperature in height intervals of 100 m were used for the calculation of Ri. As can be inferred from the profiles in Fig. 9, Ri is positive at most heights in the morning, which means stable conditions. In contrast, at noon and in the afternoon, slightly negative values of Ri (as low as − 1.3 at noon) were obtained at some heights lower than 1.0 km. This suggests the existence of local unstable layers in the ABL at those times of the day.

3.2.2 Variation of Turbulence Structures in the Boundary Layer

To examine variation in the properties of turbulence structures for the duration of periods of increased wind speed, the data series in the afternoon during 1200–1930 LST on 3 February 2016 was divided into three subcases, each having a period of 150 min (Fig. 5). This period is shorter than that of the observation case in Sect. 3.1 for the inspection of the change during the period in the afternoon. The procedure of the wavelet analysis described in Sect. 3.1 was applied to the *u* velocity component (in the horizontal plane) over five parts, which was measured by the sonic anemometer at the 25-m level. The average value of $\overline{u}$ in each subcase is 2.6, 3.8, and 2.4 m s^{-1}. In subcase 2, the wind speed ($\overline{u}$) attains to the maximum on this day.

In subcase 1 (1200–1430), the wavelet variance spectrum shows a global maximum at the time scale of 92 s and relatively small variance in the large-scale range of 100–300 s (Fig. 10, in blue). In subcase 2 (1430–1700), a local maximum is located at 56 s and the wavelet variance gradually increases as the time scale increases (Fig. 10, in purple). This increase of variance means the existence of very large velocity variations (cf. Sect. 3.1). During this period of subcase 2, further intensification of wind speed was observed by a Doppler lidar. Wavelet variance is also large in the large-scale range. Subsequently, in subcase 3 (1700–1930), the spectrum indicates a clear peak (global maximum) at 148 s in the large-scale range (Fig. 10, in brown).

At the centre (200 s) of the large-scale range, the magnitude of the wavelet variance in each subcase is 0.40, 0.56, and 0.45. The wavelet variance spectra indicate the more frequent emergence of large-scale turbulence structures in subcases 2 and 3. Regarding the stability effect (cf. Sect. 3.1), z/L is -0.9 to -0.1 for each part in subcase 2. Even so, these structures are found also in the early evening, when unstable conditions are almost absent (z/L is -0.1 to 0.8 in subcase 3). As discussed in Sect. 3.1, the predominance of large-scale turbulence structures is likely related to the evolution of the ABL. Following the development of the ABL, wind speed near the surface increases. Turbulence structures around the period of intensification of wind speed at 1430 LST are analysed below.

Measurements of three wind components by the Doppler lidar can illustrate the wind pattern of the turbulence structure. Figure 11 shows the time–height cross-sections of *u* and *w* velocity components acquired by the Doppler lidar (from the real-time acquisition data) and the time series of the same components by the sonic anemometer at the 25-m level, which were observed during 1400–1500 LST. For both instruments, *u* components were taken in the horizontal plane and *w* components were taken in the vertical axis. Moreover, *u* components at all measurement levels of the Doppler lidar unit were taken in the same direction as the

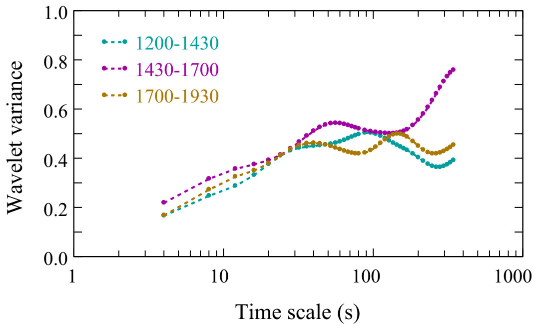

Fig. 10 Wavelet variance spectra for the *u* velocity component as a function of the time scale, obtained for three subcases during 1200–1430 (blue), 1430–1700 (purple), and 1700–1930 LST (brown) on 3 February 2016

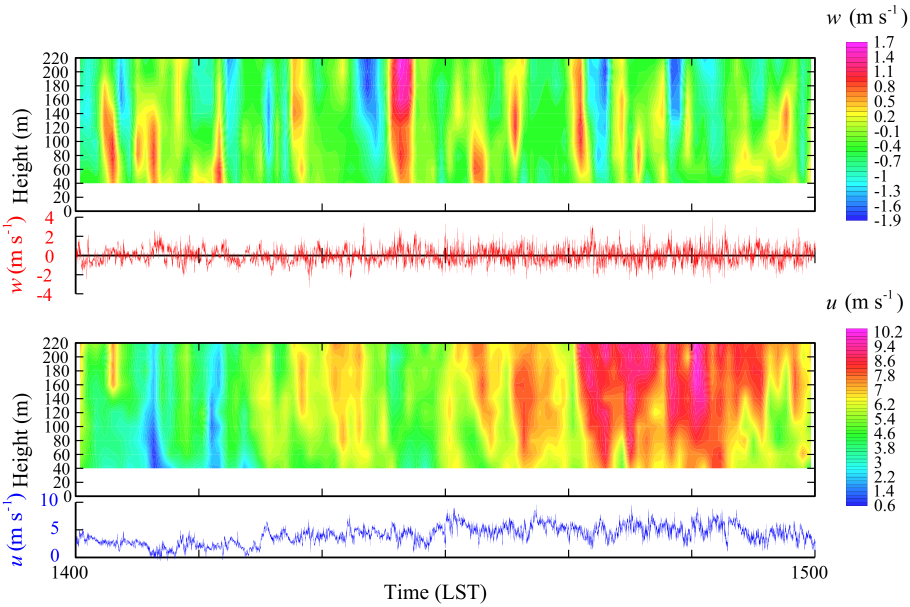

Fig. 11 *u* and *w* velocity components observed by the Doppler lidar (time–height cross-sections) and the sonic anemometer at 25 m (blue and red plots), obtained during 1400–1500 LST on 3 February 2016. The upper panel shows the *w* components, and the lower panel shows the *u* components

30-min mean wind at the lowest level (40 m). By using this process, a time–height cross-section indicates the variation of the vertical profile of the wind towards the one direction. In addition, owing to the apparent energy increase of wind speed fluctuations at high frequencies (Cañadillas et al. 2011), block averaging every 40 s was applied to the velocity components acquired by the Doppler lidar. This averaging time was selected from the comparison of power spectra between the sonic anemometer and Doppler lidar data during 1200–1530 LST.

In the upper panel of Fig. 11 (*w* components), regions of upward velocity appear intermittently. Before 1430 LST, the relation between the *u* and *w* velocity components is not clear. For example, any variation corresponding to a large positive *w* region during 1426–1427 LST is not detectable in the *u* components (lower panel of Fig. 11). As is seen from Fig. 6, the average wind speed abruptly intensified at around 1430 LST and high wind speed continued until around 1510 LST. In Fig. 11, a region of upward velocity, which extends over the whole height range, is found for a short time at around 1441 LST. The maximum *w* component in the block averages is 1.1 m s^{-1} at 120 m. A descending area of higher wind speed appears after the ascending region passed. The maximum downward velocity is 1.8 m s^{-1} at 200 m, and the maximum wind speed is 9.5 m s^{-1} at 220 m. In the surface layer (25 m), a region of upward velocity and a subsequent event of high wind speed were observed by the sonic anemometer. The estimated duration of the high-speed region is roughly 60 s; wavelet variance is large at this time-scale (Fig. 10, subcase 2 in purple). For the period 1430–1500 LST, the stability was near neutral with a small shift towards unstable conditions ($z/L = -0.1$). The wind pattern of the ascending region and descending high-speed area resembles that of the ejection–sweep structure (cf. Gao et al. 1989), which is thought to occur under a wind shear condition. This type of wind pattern was also found at another time of the day and on 10 February 2016. The estimated spatial scale of the high-speed region in this study is

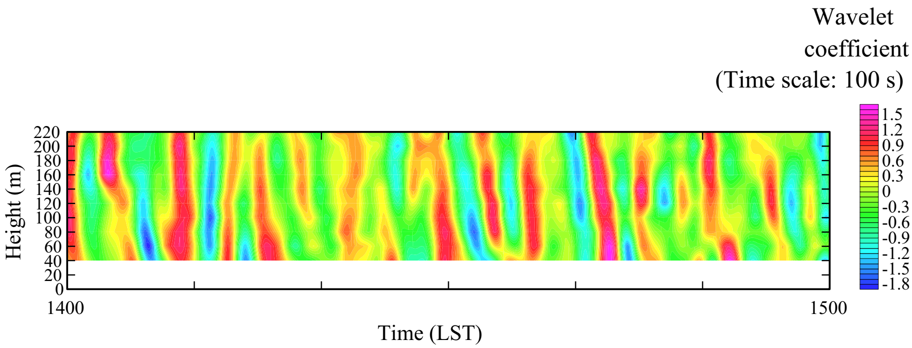

Fig. 12 Time–height cross-section of wavelet coefficients for the *u* velocity component observed by the Doppler lidar during 1400–1500 LST on 3 February 2016. The time scale for the wavelet transform is 100 s

300 m from the mean *u* at 25 m. This is considerably large in comparison with the scale of approximately 50 m at the mean forest height for the (high-speed) sweep region depicted in Gao et al. (1989).

The sonic virtual temperature in the region of upward velocity (1442 LST) shows a maximum excess of 0.6 K from the average of this part. This feature is similar to that of a plume structure forced by buoyancy (Kaimal and Businger 1970). When the layer is unstably stratified (under slightly unstable conditions), the air lifted from below is warmer than surroundings. As proposed by Horiguchi et al. (2014), the interaction of the buoyant region with the shear-driven structure may induce a larger motion. The influence of stability is likely related to the favourable conditions for the emergence of large-scale turbulence structures.

After the passage of the turbulence structure at 1441–1443 LST, high-speed areas are frequently seen in Fig. 11. For the period 1400–1500 LST, large-scale turbulence structures were extracted using the integral wavelet transform for the *u* velocity component observed by the Doppler lidar at each level. Fluctuations normalized with respect to the standard deviation in a 30-min data segment were used for the analysis. Figure 12 is a time–height cross-section of wavelet coefficients with a time-scale of 100 s, the lower limit of the scale for the large-scale turbulence structure in this study. High-speed structures, which are indicated by warm-colour (red) areas, appear intermittently over the whole period and extend vertically towards the surface. In order to detect high-speed structures, the arbitrary selected threshold of 0.5 is applied to the wavelet coefficients at the lowest level (40 m). A total of 13 structures are found in the period 1400–1500 LST. The wavelet transform analyzes localized variations of time series data irrespective of their magnitude. Low-amplitude structures existed before 1430 LST, and high-speed areas became clear in the original *u* components (Fig. 11) after the intensification of average wind speed. This result indicates that large-scale turbulence structures and the intensification of average wind speed occur in different processes.

4 Conclusions

Turbulence measurements in the surface layer and intensive observations of the ABL with various instruments were carried out during cold and windy periods in a Kyoto suburb. The roughness elements upwind of the site have some effect on the intensity of turbulence.

Under near-neutral situations, we recognized the frequent occurrence of large-scale turbulence structures with temporal scales of 100–300 s. However, the predominance of these structures is only sometimes observed in the analysed cases. Possible factors of the occurrence of large-scale turbulence structures were examined. First of all, a stability shift towards unstable conditions was seen to be favourable for the emergence of large-scale turbulence structures. Next, the predominance of those structures was related to the diurnal evolution of the ABL. These results suggest a top-down influence for the formation of large-scale turbulence structures, meaning that surrounding conditions make a large contribution.

The use of a Doppler lidar and radiosondes for the observation of higher levels has allowed us to obtain an insight into the process related to the diurnal evolution of the wind profile in the lower ABL: a high-speed layer in the upper levels extends downwards owing to turbulent mixing by wind shear and other additional mechanisms. Intermittent further intensification of wind speed was also observed. During the period of high wind speed (afternoon), large-scale turbulence structures were frequently observed. The wind pattern of these large-scale structures resembled that of the ejection–sweep structure previously observed under unstable and near-neutral conditions. Further investigations into the relation between the regions of strong winds at various scales and the turbulence structures are important subjects.

In this study, we described the characteristics obtained from observations. Having found that the emergence of large-scale turbulence structures is a prevalent feature of the ABL in this part of the Kyoto City suburbs, as a next step, we aim to analyze the observation data at other places to examine its generality.

Acknowledgements We would like to thank members of the Disaster Prevention Research Institute, Kyoto University, for their assistance in the maintenance of the measurement system and observations. This study was supported by the Japan Society for the Promotion of Science, Grant-in-Aid for challenging Exploratory Research, 24651208, 2012–2013, and Grant-in-Aid for Scientific Research (B), 26282107, 2014–2016.

References

Arya SP (2001) Introduction to micrometeorology, 2nd edn. Academic Press
Cañadillas B, Westerhellweg A, Neumann T (2011) Testing the performance of a ground-based wind lidar system: one year intercomparison at the offshore platform FINO1. DEWI Magazin 38:58–64
Chen J, Hu F (2003) Coherent structures detected in atmospheric boundary-layer turbulence using wavelet transforms at Huaihe River basin, China. Boundary-Layer Meteorol 107:429–444
Collineau S, Brunet Y (1993) Detection of turbulent coherent motions in a forest canopy part I: wavelet analysis. Boundary-Layer Meteorol 65:357–379
Crawford KC, Hudson HR (1973) The diurnal wind variation in the lowest 1500 ft in Central Oklahoma: June 1966-May 1967. J Appl Meteorol 12:127–132
Feigenwinter C, Vogt R (2005) Detection and analysis of coherent structures in urban turbulence. Theor Appl Climatol 81:219–230
Foken T (2008) Micrometeorology. Springer-Verlag
Gao W, Shaw RH, Paw UKT (1989) Observation of organized structure in turbulent flow within and above a forest canopy. Boundary-Layer Meteorol 47:349–377
Gao W, Li BL (1993) Wavelet analysis of coherent structures at the atmosphere–forest interface. J Appl Meteorol 32:1717–1725
Garratt JR (1994) The atmospheric boundary layer. Cambridge University Press
Gottschall J, Courtney M (2010) Verification test for three Windcube^{TM} WLS7 LiDARs at the Høvsøre test site. Tech Rep Risø-R-1732(EN)
Grimmond CSB, Oke TR (1999) Aerodynamic properties of urban areas derived from analysis of surface form. J Appl Meteorol 38:1262–1292
Horiguchi M, Hayashi T, Adachi A, Onogi S (2012) Large-scale turbulence structures and their contributions to the momentum flux and turbulence in the near-neutral atmospheric boundary layer observed from a 213-m tall meteorological tower. Boundary-Layer Meteorol 144:179–198

Horiguchi M, Hayashi T, Adachi A, Onogi S (2014) Stability dependence and diurnal change of large-scale turbulence structures in the near-neutral atmospheric boundary layer observed from a meteorological tower. Boundary-Layer Meteorol 151:221–237
Hunt JCR, Morrison JF (2000) Eddy structure in turbulent boundary layers. Eur J Mech B 19:673–694
Hutchins N, Marusic I (2007) Evidence of very long meandering features in the logarithmic region of turbulent boundary layers. J Fluid Mech 579:1–28
Hutchins N, Chauhan K, Marusic I, Monty J, Klewicki J (2012) Towards reconciling the large-scale structure of turbulent boundary layers in the atmosphere and laboratory. Boundary-Layer Meteorol 145:273–306
Inagaki A, Kanda M, Ahmad NH, Yagi A, Onodera N, Aoki T (2017) A numerical study of turbulence statistics and the structure of a spatially-developing boundary layer over a realistic urban geometry. Boundary-Layer Meteorol 164:161–181
Jiménez PA, Vilà-Guerau de Arellano J, Dudhia J, Bosveld FC (2016) Role of synoptic- and meso-scales on the evolution of the boundary-layer wind profile over a coastal region: the near-coast diurnal acceleration. Meteorol Atmos Phys 128:39–56
Kaimal JC, Businger JA (1970) Case studies of a convective plume and a dust devil. J Appl Meteorol 9:612–620
Kaimal JC, Finnigan JJ (1994) Atmospheric boundary layer flows. Oxford University Press
Kim HT, Kline SJ, Reynolds WC (1971) The production of turbulence near a smooth wall in a turbulent boundary layer. J Fluid Mech 50:133–160
Kim KC, Adrian RJ (1999) Very large-scale motion in the outer layer. Phys Fluids 11:417–422
Kronland-Martinet R, Morlet J, Grossmann A (1987) Analysis of sound patterns through wavelet transforms. Int J Patt Recogn Artif Intell 1:273–302
Larsén XG, Larsen SE, Petersen EL (2016) Full-scale spectrum of boundary-layer winds. Boundary-Layer Meteorol 159:349–371
Lenschow DH, Wyngaard JC, Pennell WT (1980) Mean-field and second-moment budgets in a baroclinic, convective boundary layer. J Atmos Sci 37:1313–1326
Mahrt L (1981) The early evening boundary layer transition. Q J R Meteorol Soc 107:329–343
Mahrt L (1991) Eddy asymmetry in the sheared heated boundary layer. J Atmos Sci 48:472–492
Newsom R, Calhoun R, Ligon D, Allwine J (2008) Linearly organized turbulence structures observed over a suburban area by dual-Doppler lidar. Boundary-Layer Meteorol 127:111–130
Novitskii MA, Gaitandzhiev DE, Mazurin NF, Matskevich MK (2011) Turbulence characteristics in the coastal zone with breeze circulation. Russ Meteorol Hydrol 36:580–589
Park SB, Baik JJ, Han BS (2015) Large-eddy simulation of turbulent flow in a densely built-up urban area. Environ Fluid Mech 15:235–250
Roth M (2000) Review of atmospheric turbulence over cities. Q J R Meteorol Soc 126:941–990
Stewart ID, Oke TR (2012) Local climate zones for urban temperature studies. Bull Am Meteorol Soc 93:1879–1900
Stull RB (1988) An introduction to boundary layer meteorology. Kluwer Academic Publishers
Van der Hoven I (1957) Power spectrum of horizontal wind speed in the frequency range from 0.0007 to 900 cycles per hour. J Meteorol 14:160–164
Wang GH, Zheng XJ (2016) Very large scale motions in the atmospheric surface layer: a field investigation. J Fluid Mech 802:464–489
Yagi A, Inagaki A, Kanda M, Fujiwara C, Fujiyoshi Y (2017) Nature of streaky structures observed with a Doppler lidar. Boundary-Layer Meteorol 163:19–40
Yoshida T, Takemi T, Horiguchi M (2018) Large-eddy-simulation study of the effects of building-height variability on turbulent flows over an actual urban area. Boundary-Layer Meteorol 168:127–153